INVESTIGATION OF VORTEX-GENERATOR INDUCED FLOW STRUCTURES ON A FLAT PLATE USING IR THERMOGRAPHY, PARTICLE IMAGE VELOCIMETRY AND OIL FLOW VISUALIZATION

Alexander SCHUKMANN, Christian LANDFESTER,
Martin BÖHLE

Technische Universität Kaiserslautern, Gottlieb-Daimler-Straße 44,
67663 Kaiserslautern, Germany

SUMMARY

The use of passive flow control, e.g. by means of vortex generators attached to the blade or endwall surface, is one approach to reduce boundary layer separation induced aerodynamic losses in axial fans by separation point delay. To enhance the understanding of the involved flow phenomena, this work presents a detailed study of the flow on a flat plate using several conventional vortex generator geometries. The experiments are conducted in a open-loop cascade wind tunnel at a fixed turbulence intensity of 1.5%. The surface flow is investigated using oil flow visualization and infrared (IR) thermography utilizing the dependency of wall heat transfer on local flow characteristics. For an insight into the three-dimensional flow field, Particle Image Velocimetry (PIV) measurements were conducted on several planes parallel to the main flow direction.

INTRODUCTION

The insertion of disruptive bodies into a flow often influences its trajectory in a significant and complex way. Using as an example the flow around a vertical cylinder (cf. figure 1), flow structures that typically arise as well as the terminology utilized in the further course will be introduced.
Due to the top-down decreasing stagnation pressure on the surface of the cylinder caused by the vertical velocity gradient of the incoming flow, a downward flow movement occurs on its windward side. At the same time, a horizontal boundary layer separation starts at the base of the cylinder, indicated by the dashed separation line S around the cylinder base. Interacting with the windward down flow, this boundary layer separation leads to the formation of a so called horseshoe vortex system, that is drawn further downstream on both sides of the cylinder into the wake region. Due to the displacement of the external flow, a contraction of the streamlines occurs at the outer edge of the horseshoe vortex. Furthermore, boundary layer separation on the cylinder surface results in the formation of vortex structures in the wake [1].

Vortex generators were first described by Taylor [2] in the late 1940s and have been in use for many years. On the one hand, their effect is based on a momentum transfer of the high-energy external flow

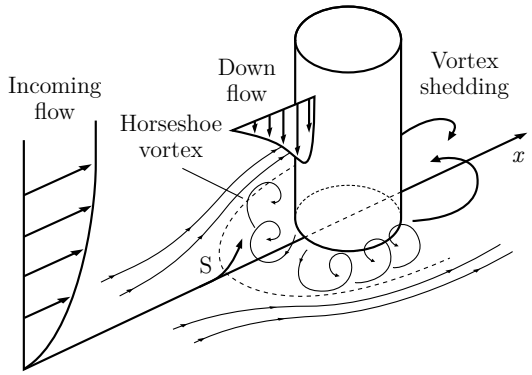

Fig 1: Flow structures around a cylinder (based on [1])

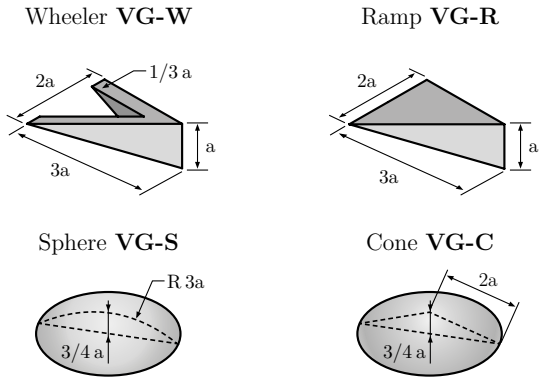

Fig 2: Vortex generator designs

into the boundary layer [3]. On the other hand, disruptive bodies can create flow instabilities that force a preliminary laminar-turbulent transition which is associated with increased momentum transfer [4]. The effect of such disruptive bodies, or the vortex structures created when they interact with a flow, typically find application in the prevention of flow separation due to adverse pressure gradients in fluid machinery impellers, such as fans and compressors [5] [6] [7], wind turbines [8] [9], in the automotive sector [10] and on aircraft wings and fuselages [11] [12] [13]. Other applications include increasing the effectiveness of heat exchangers [14] and gas turbine combustors [15].
The use of IR thermography for the investigation of convective heat transfer as well as the analysis of complex wall-bounded flows has been increasingly applied for several years [16]. An examination of laminar-turbulent transition on a airfoil using IR thermography is provided by Joseph et al. [17]. This method based on differences in surface temperatures caused by variations in the surface heat transfer rate associated with laminar and turbulent boundary layers.
In this study, four distinct generic vortex generator designs (hereafter VG) serve as test objects, whose geometric properties related to a shape parameter a and naming can be taken from figure 2. The V-shaped variant *wheeler sharp* refers to [18]. The vortex generators were manufactured from a polymer on an in-house 3D printer using a multi-jet printing process. The generators VG-W and VG-R were additionally used in a 180° rotated configuration.

EXPERIMENTAL SETUP AND PROCEDURE

The experimental investigations were carried out at ambient temperature (20 °C) in the institute's own open loop wind tunnel with a 500×200 mm rectangular outlet cross section. The measuring section is shown in figure 3. More details on the setup and specifications of the tunnel can be taken from [19]. The vortex generators are mounted on a flat plate, which is clamped between two polymethyl methacrylate (PMMA) walls at the outlet of the tunnel in a rotatable frame holder. By slightly adjusting the plate in the flow in terms of pitch angle, observed detachment bubbles in the leading edge region can be avoided. By means of a turbulence grid installed upstream of the outlet area, a constant turbulence intensity of 1.5% is ensured over all feasible Reynolds numbers, which was confirmed by hot-wire anemometry prior to the investigations. All investigations were performed for three distinct Reynolds numbers $Re_1 = 2000$, $Re_2 = 4000$, $Re_3 = 6000$ formed with the characteristic measure of vortex generators $2a = 16$ mm, cf. figure 2.

Infrared thermography setup

Also shown in figure 3 is the camera mount for the infrared (IR) camera system at the upper end of the frame with an indicated aperture angle. The camera is a Infratec VarioCAM HDx head 600 with an uncooled microbolometer and detector format of 640×480. The temperature measurement range of the camera is -40 °C to 600 °C with an absolute measurement accuracy of $\pm 2\%$ and a relative temperature resolution of up to 0.03 °C at 30 °C.

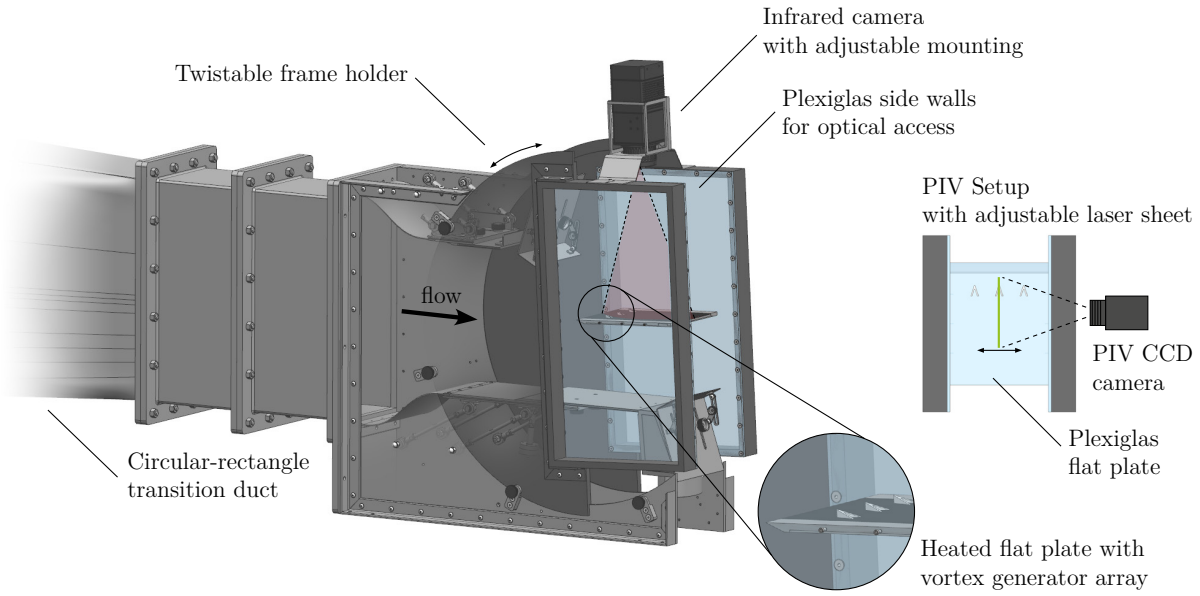

Figure 3: Test section

The multi-part plate (see figure 4 for details) consists of a copper base body ($\lambda = 401\,\mathrm{W\,m^{-1}\,K^{-1}}$), to which self-adhesive polyester heating foil ($\dot{q} = 1330\,\mathrm{W\,m^{-2}}$) was attached to the bottom side. A Teflon coating (emissivity $\varepsilon = 0.92$, thickness $d = 0.5\,\mathrm{mm}$, $\lambda = 0.25\,\mathrm{W\,m\,K^{-1}}$) was applied to the top site of the copper plate. This Teflon coating serves as thermal insulation to limit the heat flux through the copper plate, resulting in homogeneous heat penetration through the copper base body. Due to the large temperature gradient (approx. $6600\,\mathrm{K\,m^{-1}}$) in the z direction from the bottom to the flow-facing side of the coating, a 1D heat flux is imposed, ensuring that flow-induced differences in convective heat transfer dominate the temperature distribution on the top surface. The convective heat transfer depends on the local temperature gradient in the immediate vicinity of the wall. Due to the increased momentum and heat exchange, a steeper temperature gradient is present in turbulent boundary layers compared to laminar boundary layers. Therefore, higher heat transfer coefficients and thus lower surface temperatures are to be expected in turbulent boundary layers - all other conditions being equal. Furthermore, the heat transfer is significantly influenced by secondary flows (e.g. due to impingement cooling effects). A cavity between the heated copper plate and the support structure serves as thermal insulation against the support structure. Six thermocouples were integrated along the center line to monitor the temperature on the bottom. To reduce the measurement uncertainty due to noise, 100 single IR measurements were averaged for each configuration.

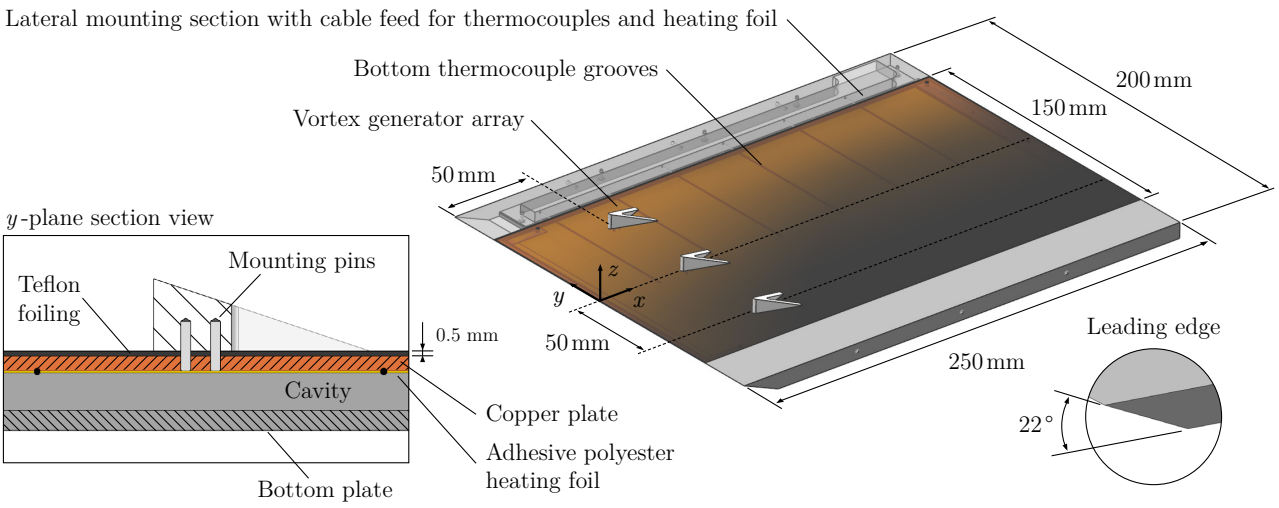

Figure 4: Detail view of heated flat plate including mounted vortex generators

Particle image velocimetry setup

PIV investigations were performed on several y-planes in the main flow direction for $Re = 2000$ and $Re = 6000$ using a Dantec Dynamics measurement system. To avoid unwanted reflections, the multi-part plate was replaced by a PMMA plate with identical dimensions. The PIV system consists of a Q-switched double-pulsed Nd:YAG laser with a maximal pulse energy of 140 mJ at 532 nm and a charge-coupled device double frame camera (2048×2048 px) whose optical access to the test section is ensured by the PMMA side walls. For the PIV setup, the laser was mounted horizontally on a linear guideway above the test section instead of the IR camera, which allows adjustment in the y-direction. The laser beam was deflected here with 90° optics. The field of view in the physical plane measured 90×90 mm to allow for a high-resolution investigation of the near wake flow. The system was operated with a repetition rate of 5 Hz and time-between-pulses (TbP) was set to 20 µs for the high Reynolds number case and 60 µs for the low Reynolds number case to maintain an average particle displacement of approximately 6 px in the main flow. A water-glycol-based fog fluid (particle size 2 µm) was used as the seeding material and introduced at the inlet nozzle of the channel. Here, an average particle density of 0.006 particles per pixel was obtained in the 2 mm thick laser sheet. The image data (200 images per measurement for statistical convergence) were analyzed using an adaptive algorithm with multi-grid cross correlation and averaged over time. Here, the size of the smallest interrogation area was chosen to be 32×32 px.

Oil flow visualization setup

A mixture of petroleum and fluorescent pigment in a ratio of 5:1 with the addition of oleic acid was used for the oil flow visualizations. To improve the contrast ratio, another blackened plate was installed for the study and illuminated with two UV LED. Significant flow structures were highlighted in the analysis to clarify the flow topology.

RESULTS

To quantify the influence of the vortex generators on the local heat transfer, the temperature distribution on the plate without vortex generators was first determined for the three Reynolds numbers mentioned above. The reference temperature distribution T_{REF} without airflow was used for normalization to address local inhomogeneities of the power output of the heating foil.
Figure 5 depicts the streamwise development of the normalized temperature T/T_{REF} (in degree Celsius) averaged in the y direction. Here it can be seen that the temperature initially increases in all three cases. It can be assumed that the initially laminar boundary layer heats up and becomes thermally saturated in streamwise direction. At the same time, the local temperature gradient flattens in flow direction due to boundary layer thickening. Both effects explain the initial temperature rise. From

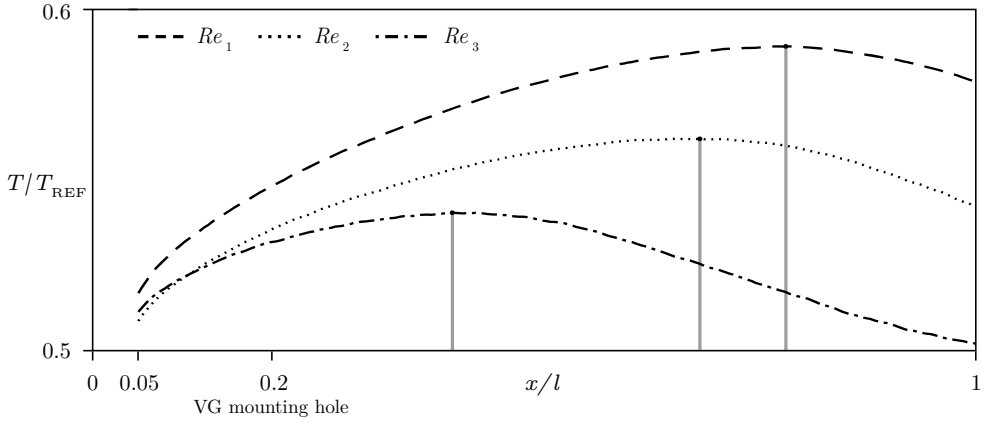

Figure 5: Normalized temperature distribution for free transition, local maxima marked with solid line

a certain point dependent on the Reynolds number, the temperature drops steadily until the end of the plate. RANS-based CFD calculations performed in parallel to the experiments using the k-ω-SST transitional turbulence model according to [20] support the assumption that the temperature drop is associated with a laminar-turbulent transition (free transition). As expected, the transition region moves upstream for larger Reynolds numbers. The over-all temperature offset between the three Reynolds numbers can be traced back to their influence on the boundary layer thickness.

Influence of the vortex generator design

The following figures show the results of the respective vortex generators for $Re = 6000$. The local temperature distribution from the IR measurement was normalized with the corresponding temperature distribution of the free transition to quantify the effect of vortex generator induced disturbances. The results of the PIV measurements for each of two cutting planes are shown as a normalized velocity distribution in the x-z direction with superimposed streamlines. The position of the cutting planes is marked as dashed lines in the thermogram.

VG-W In the installation direction originally intended by Wheeler (cf. figure 6), the following flow topologies can be seen: In the oil flow pattern, a stagnation zone can be seen in the leading edge region, which is strongly constricted by the diverted main flow along both shanks. Due to the convergence of the streamlines, the formation area of the dominating wake vortices, which are clearly visible in the two PIV planes, can be assumed here. As these two vortices originate separate from each other at the flanks of the shanks, it would be misleading to use the term horseshoe vortex. In the inner region of the two shanks, a weak downflow can be seen behind the recirculation zone.
In the wake, a cavity is formed between the dominating vortices and the plate, marked by diverging streamlines immediately behind the vortex generator spreading out from the center line. Due to the momentum exchange of the trapped air inside the cavity with the two dominating vortices, it is reasonable to assume that the formation of a further inner vortex system with reversed direction of rotation sets in. However, the course of the streamlines suggests that this vortex system has a significantly reduced vorticity. While the recirculation zone in the forefront of the vortex generator can be recognized by the reduced heat transfer, the formation zone of the wake vortices is characterized by an increased heat transfer. The zone of diverging streamlines within the cavity formed by the two main vortices is accompanied by a further rise of the local heat transfer, which weakens and widens significantly in the far wake. It is noteworthy that this zone propagates downstream in a triangular shape, which is characteristic for turbulent disturbances, beyond the zone of influence of secondary flows evident in the oil flow pattern. It can be assumed that the vortex generator enforces the forma-

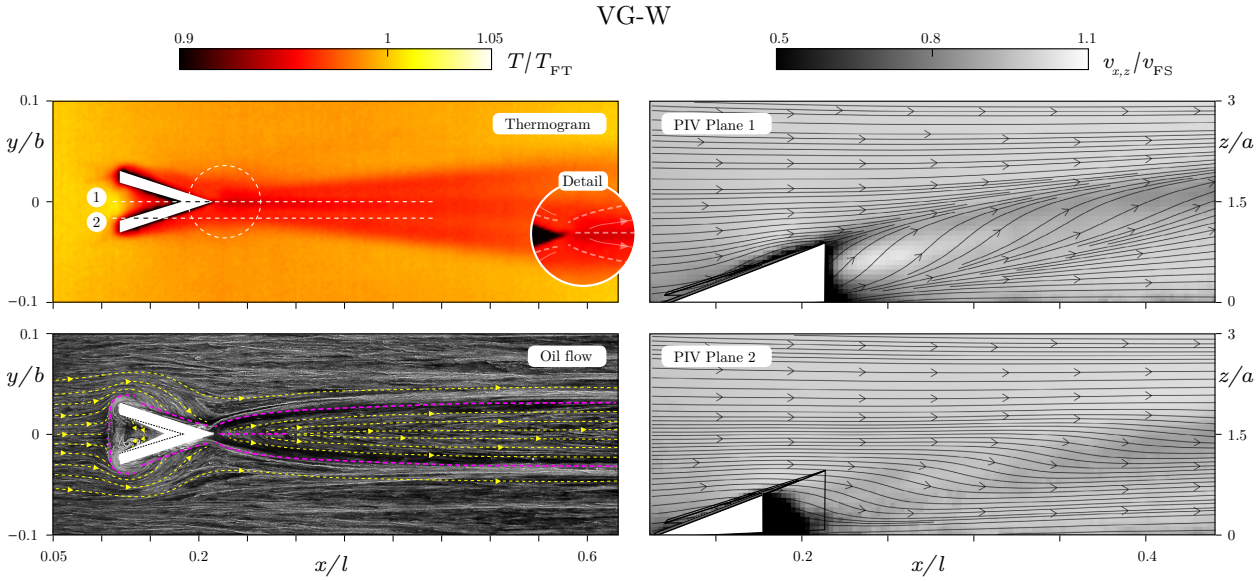

Figure 6: Thermogram, oil flow visualization and PIV measurement for VG-W

tion of a turbulent wedge associated with increased heat transfer due to turbulent fluctuation motions. The PIV measurement shows that the dominating vortices already lift off the plate in the near wake and mix significantly with the main flow in the far wake. Therefore, these structures cannot be made out in the oil flow visualization. Immediately behind the vortex generator, a dead wake is visible on the center line. In the area of the vortex formation zone behind the shank of the vortex generator (plane 2), the flow velocities in x-z-direction are also significantly reduced. Due to the presumably low vorticity, the inner vortex system in the cavity cannot be identified in the PIV section plane.

VG-W-180 Figure 7 shows the results of the 180° rotated Wheeler variant, which differs significantly with respect to the flow topology. In the oil flow image, a clear stagnation zone can be seen in the area of the leading edge. Here, the incoming main flow is deflected by the downstream flow at both shanks of the vortex generator. The outer streamlines are compressed due to deflection of the main flow. The wake is characterized by a symmetrical distribution of secondary flows, which are dominated by a strongly widening pair of vortices, which is enclosed by the deflected main flow. Two prominent separation lines leading downstream from the inner trailing edges of the shanks can be identified by the convergence of the streamlines and the accumulation of paint. A cavity, which is enclosed by the two vortices and widens further downstream, can be identified between the inner reattachment lines indicated by diverging streamlines. Due to the backward sloping, triangular structure of the vortex generator, fluid is transported downward and settles on the plate behind the shank trailing edges. A recirculation zone identifiable by an accumulation of paint can be seen between the two shanks. It is separated by a region of radially diverging streamlines indicating an impinging downflow from the inner flanks of the two shanks.
In the thermogram, the stagnation zone is recognizable by a clear and sharply defined reduction in surface temperature. The downflow apparently transports colder air close to the wall and generates an increased heat transfer via an impingement cooling effect. The interaction of the secondary flow results in sharply defined temperature zones in the wake region (see detail). The area of vortex separation is characterized by a reduced heat transfer. In the area of the vortex root as well as in the area of the contact zone behind the two trailing edges, an increased heat transfer can be seen. While the downstream flow between the shanks generates the highest heat transfer, the neighboring recirculation zone is associated with a local temperature increase. The cavity, which is enclosed by the two vortices, shows a reduced temperature. The triangular shape of the outer region of increased heat transfer propagates downstream beyond the zone of influence of the secondary flows as it was already discussed for the 0° Wheeler variant. In the PIV plane along the center line, the stagnation zone in front of the vortex generator is characterized by reduced flow velocities. As the main flow follows the

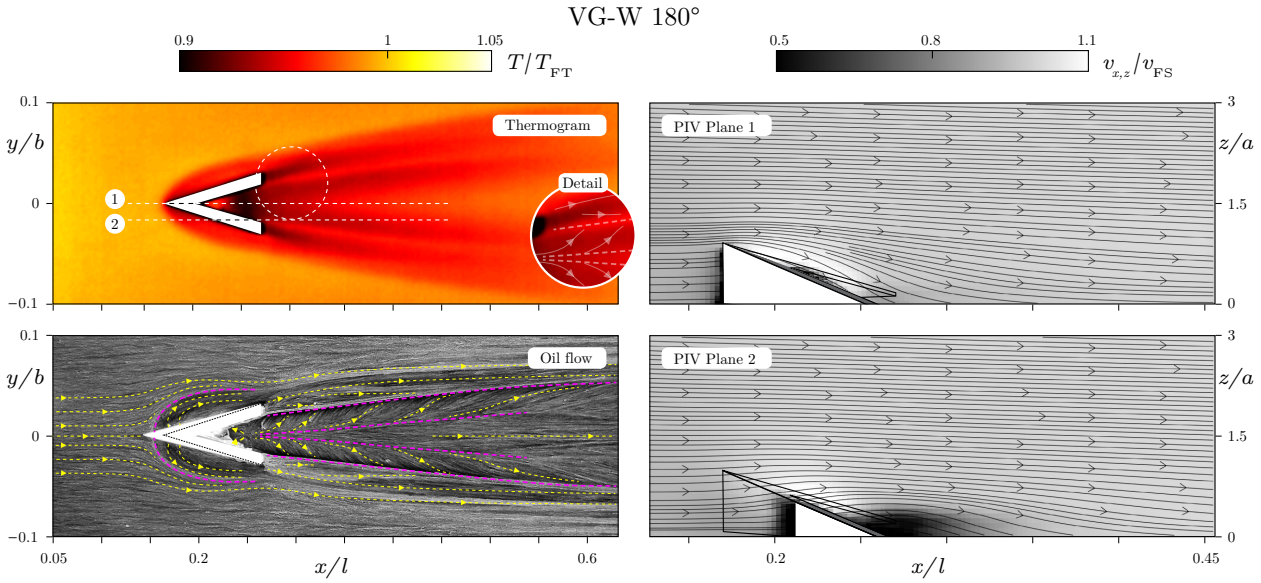

Figure 7: Thermogram, oil flow visualization and PIV measurement for VG-W-180°

descending contour of the vortex generator, it experiences significant acceleration before reattaching to the plate. In PIV plane 2, the stagnation zone extending from the leading edge to the shank of the vortex generator, is clearly visible. Downstream, the PIV plane intersects the detachment zone of the wake vortex. It is characterized by a significant reduction in flow velocities and a deflection of the external flow – recognizable by the densification of the streamlines. The resolution of smaller scale flow phenomena, which can be seen in the thermogram and the oil flow image, is not possible with the given PIV setup.

VG-R Figure 8 shows the results of the ramp in 0° as well as in 180° position. Due to the expected similarities of the flow topology to the Wheeler geometry, the PIV results were not shown here. The stagnation zone is more pronounced in the 0° position, since the flow cannot penetrate into the space between the two shanks of the Wheeler geometry. The thermogram shows a broadening of the triangular zone of increased heat transfer compared to the Wheeler geometry. This indicates a growth in terms of turbulent fluctuation motion. The distinct secondary flow structures elucidated in the previous section are also apparent in the oil flow pattern as well as in the thermogramm. In the 180° position, a widened wake can also be seen in the oil flow pattern. The thermogram shows a zone

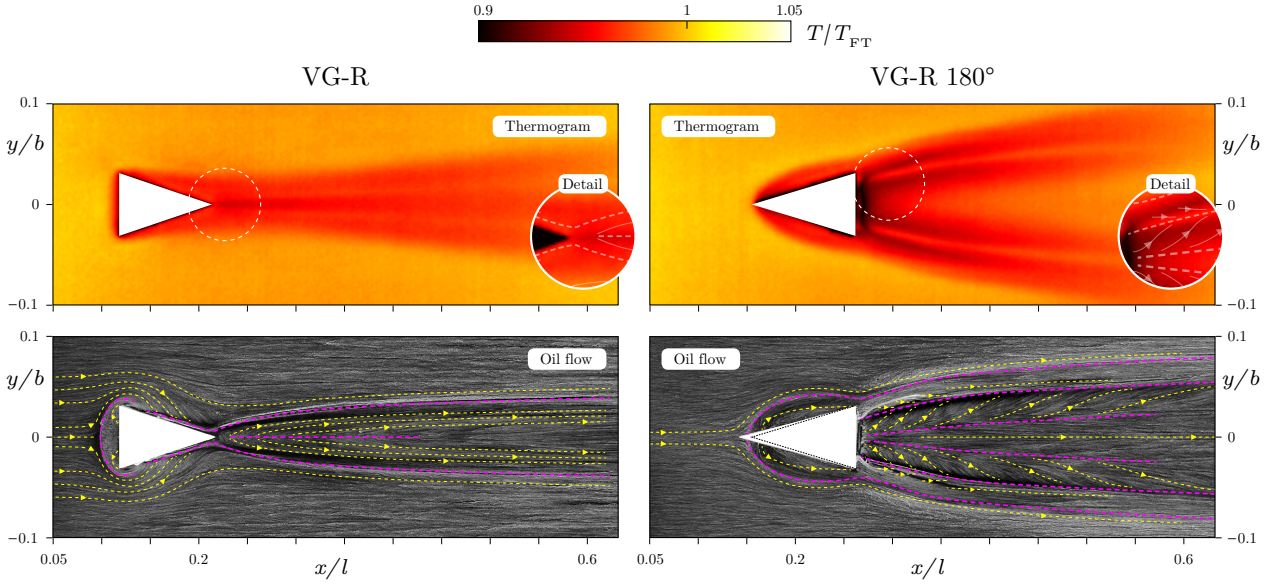

Figure 8: Thermogram and oil flow visualization for VG-R and VG-R-180°

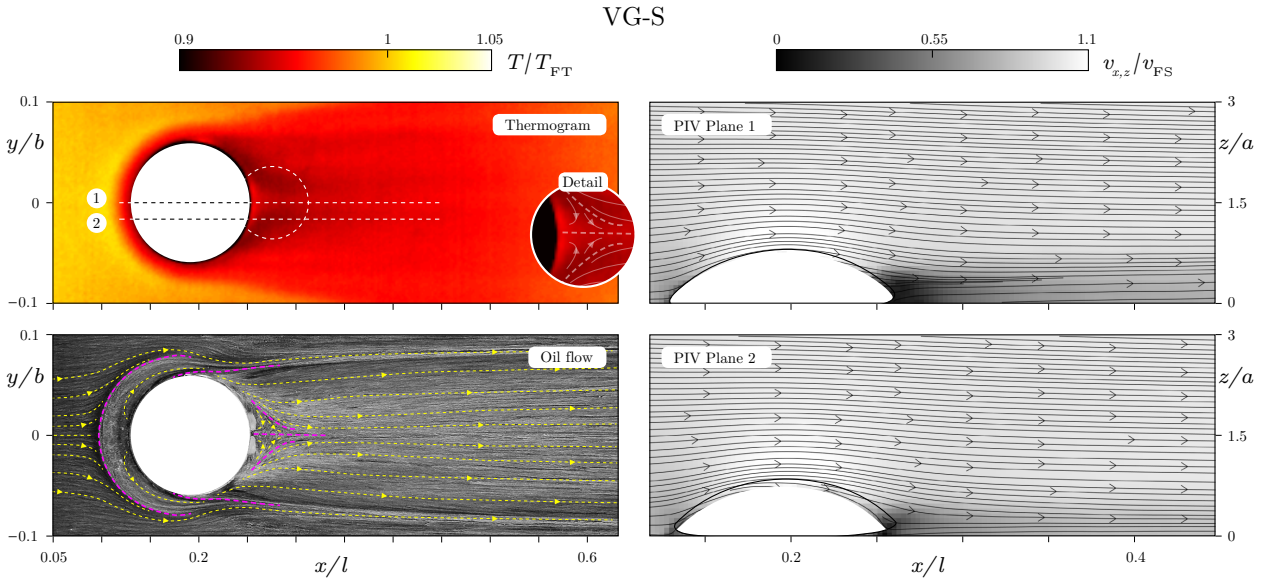

Figure 9: Thermogram, oil flow visualization and PIV measurement for VG-S

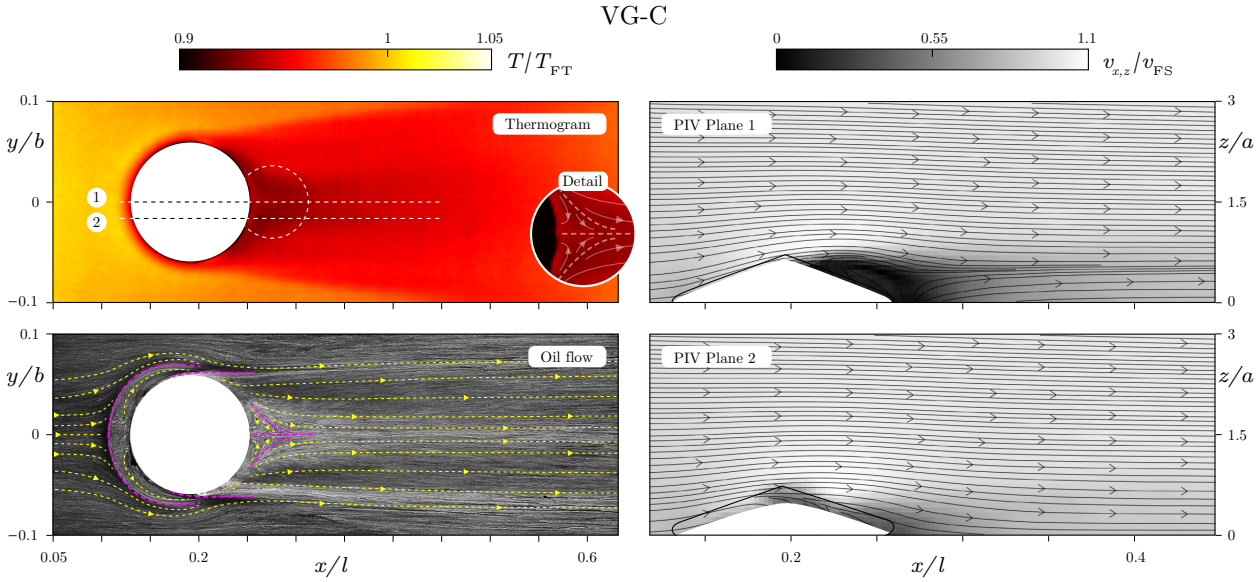

Figure 10: Thermogram, oil flow visualization and PIV measurement for VG-C

of significantly increased heat transfer in immediate proximity to the ramp trailing edge, which can be explained by impingement cooling by the downward flow.

VG-S The results of the investigation of the sphere are shown in figure 9. In the oil flow visualization as well as in the thermogram, the upstream influence of the sphere is clearly evident. Behind the saddle point, two distinct zones can be distinguished: The downflow from the surface of the sphere, which is deflected downstream along the sphere edge, results in an increased heat transfer. Between this area and the saddle point, a recirculation zone becomes apparent, which can be recognized in the oil flow image by the densification of the paint. In the thermogram, this area is characterized by reduced heat transfer. In the wake, the main flow along the center line cannot follow the sloping contour of the sphere and, therefore, separates (cf. PIV plane 1). As a result, one part of the lateral downflow heading towards the center line enters the cavity and forms a recirculation zone with reduced flow velocities. This recirculation zone is characterized by a significant accumulation of the oil paint and a reduction in heat transfer. The highest heat transfer can be seen where the lateral flow attaches onto the plate. Here, again, the triangular zone of increased heat transfer extends well beyond the secondary flows visible in the oil flow image. The PIV measurement shows a considerable acceleration of the main flow above the sphere.

VG-C The near-wall flow topology of the cone (cf. figure 10) shows very close similarities with that of the sphere. In the forefront of the cone, the recirculation area and the downflow become visible in both thermogram and oil flow visualization. However, the area of influence of the cone is reduced due to the flatter inclination compared to the sphere. This causes a reduced stagnation pressure gradient limiting the downflow. On the contrary, the lee side flow separates much sooner (see PIV level 1), causing the recirculation area to grow and shift significantly further upstream. An accumulation of oil paint is therefore not present.

Influence of Reynolds number

Figure 11 shows the normalized thermograms of ramp and sphere for the three Reynolds numbers investigated. Here, an additional averaging in y-direction was performed. The influence of secondary flow on the heat transfer described in the previous chapter can be identified for all three Reynolds numbers. A qualitative change of the flow regime can only be expected at significantly lower Reynolds numbers. On all thermograms, the triangular region of increased heat transfer, associated with a laminar-turbulent transition in the boundary layer, is evident. It is noteworthy here that the opening angle of the triangular zone increases with rising Reynolds numbers. Accordingly, the turbulent

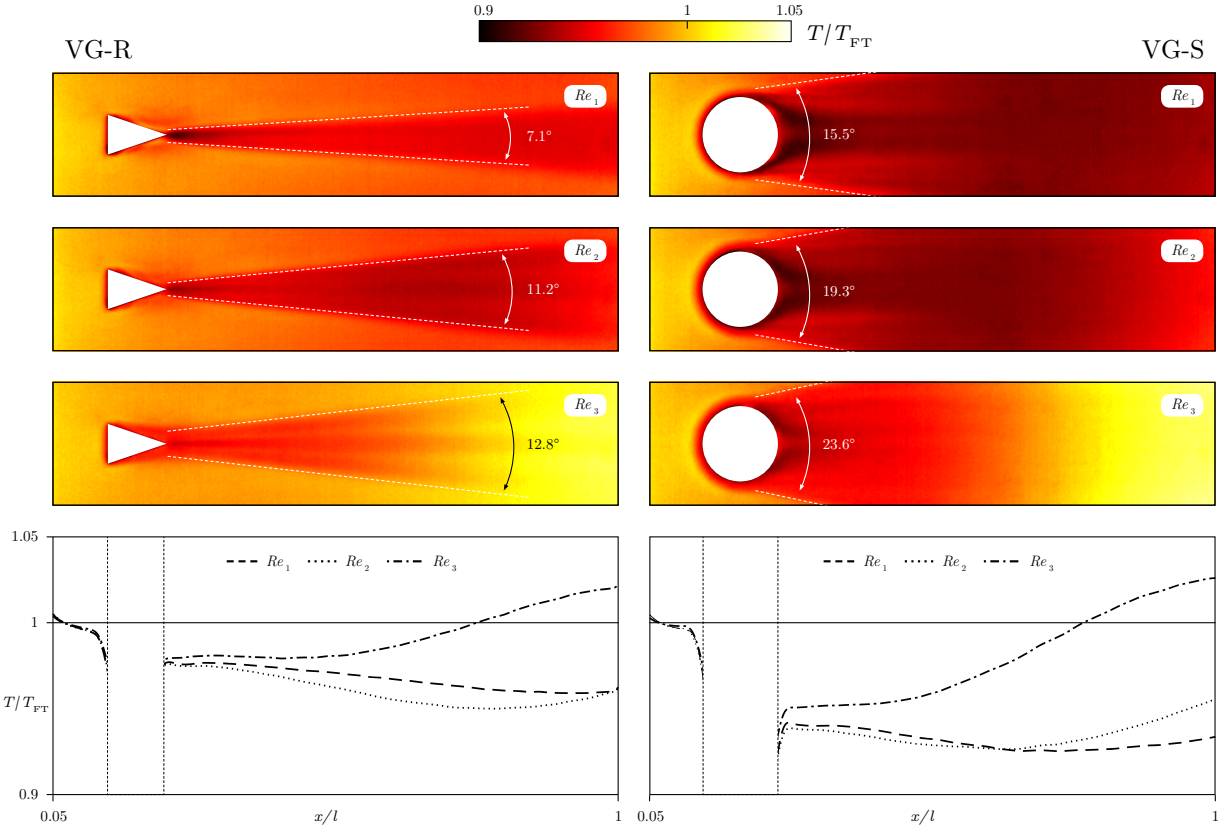

Figure 11: Reynolds number comparison of temperature distribution for VG-R und VG-S

disturbances propagate faster for larger Reynolds numbers relative to the flow velocity. This behavior can be observed for all investigated vortex generators.
The averaged temperature curves show that the heat transfer is initially increased for all Reynolds numbers compared to the level of free transition. As explained in the previous sections, this has to be attributed to the induced secondary flows as well as the enforced transition. Further downstream, however, the normalized temperatures re-approach the level of the free transition with dependence on the Reynolds number. For $Re = 6000$, the normalized temperature even surpasses the level of the free transition. It can be assumed that the early stage forced transition causes the boundary layer to thicken significantly and isolate the hot plate from the cooler mainstream in the far wake. In case of the free transition, the boundary layer is already turbulent, but the thickening has not yet set in.

CONCLUSIONS AND OUTLOOK

In this study, the effect of different vortex generator designs on a flat plate boundary layer was investigated using IR thermography, oil flow visualization technique and particle image velocimetry. It was shown that IR thermography as a non-contact method is a useful supplementary experimental approach as it provides a detailed insight into the near-wall flow conditions mediated by their influence on the local heat transfer. In contrast, the PIV measurements with the given setup facilitate the understanding of the external flow. However, phenomena close to the wall can only be insufficiently resolved due to the residual reflections of the laser sheet. To minimize these effects, the use of fluorescent coating, e.g. Rhodamine, in conjunction with a narrow-band optical filter should be considered (cf. [21]). However, the health risks associated with handling this paint must be taken into account. The study further demonstrated that oil flow visualization is still a useful and cost-effective method for investigating complex near-wall flow structures.
The assessment of the measurement results has shown that the flow around the vortex generators generates complex flow topologies that are similar to the flow around a cylinder. Here, the downflow

along the surface is significantly involved in the development of the secondary flow. However, the IR thermography results indicate that the vortex generators enforce a laminar-turbulent transition in the boundary layer which extends beyond the direct influence of the secondary flows. These turbulent disturbances propagate faster for larger Reynolds numbers relative to the flow velocity. Turbulence intensity measurements with an laser Doppler anemometry system are planned to verify this hypothesis. In addition, stereo PIV measurements are intended, which allow a measurement perpendicular to the main flow direction and, therefore, provide detailed insight into the topology of the secondary flows. In order to determine the influence of vortex generators on the separation behavior and to understand the underlying flow mechanisms, the experimental setup will be applied to a generic airflow profile for a future study.

NOMENCLATURE

a	Characteristic vortex generator length in mm
b	Width of heated part of flat plate in mm
d	Coating thickness in mm
ε	Surface emissivity of coating
l	Length of flat plate in mm
λ	Heat conductivity in $\mathrm{W\,m^{-1}\,K^{-1}}$
Re	Reynolds number
T	Surface Temperature in °C
T_{REF}	Temperature of reference case in °C
T_{FT}	Temperature of free transition case in °C
$\dot{q}$	Heat flux density of heating foil in $\mathrm{W\,m^{-2}}$
v	Velocity in $\mathrm{m\,s^{-1}}$
v_{FS}	Free stream Velocity in $\mathrm{m\,s^{-1}}$
xyz	Cartesian coordinates

REFERENCES

[1] A. Roulund, B. M. Sumer, J. Fredsoe, and J. Michelsen. Numerical and experimental investigation of flow and scour around a circular pile. *Journal of Fluid Mechanics*, 2005.

[2] H. D. Taylor. The elimination of diffuser separation by vortex generators. Technical report, United Aircraft Corporation, 1947.

[3] J. C. Lin. Review of research on low-profile vortex generators to control boundary-layer separation. *Progress in Aerospace Sciences*, 38(4-5):389–420, may 2002.

[4] R. J. Volino. Passive flow control on low-pressure turbine airfoils. *Journal of Turbomachinery*, 125(4):754–764, oct 2003.

[5] Lanier. Vortex generator for centrifugal fans, 1986.

[6] A. M. Diaa, M. F. El-Dosoky, M. A. Ahmed, and O. E. Abdel-Hafez. Boundary layer control of an axial compressor cascade using nonconventional vortex generators. In *Volume 1: Advances in Aerospace Technology*. American Society of Mechanical Engineers, nov 2015.

[7] A. M. Diaa, M. F. El Dosoky, and M. A. Ahmed. Enhancing the performance of an axial compressor cascade using vortex generators. *Journal of Aeronautics & Aerospace Engineering*, 05(04), 2016.

[8] L. Zhang, X. Li, K. Yang, and D. Xue. Effects of vortex generators on aerodynamic performance of thick wind turbine airfoils. *Journal of Wind Engineering and Industrial Aerodynamics*, 156:84–92, sep 2016.

[9] M. Chen, Z. Zhao, H. Liu, T. Wang, L. Meng, J. Feng, R. Jiang, and D. Wang. Research on the parametric modelling approach of vortex generator on wind turbine airfoil. *Frontiers in Energy Research*, 9, aug 2021.

[10] A. Yadav, P. Rawal, and R. K. Mishra. Modelling and simulation of aerodynamic performance of vortex generators for hatch back type cars. *Vibroengineering PROCEDIA*, 21:131–136, dec 2018.

[11] W. Calarese, W. Crisler, and G. Gustafson. Afterbody drag reduction by vortex generators. In *23rd Aerospace Sciences Meeting*. American Institute of Aeronautics and Astronautics, jan 1985.

[12] M. B. Bragg and G. M. Gregorek. Experimental study of airfoil performance with vortex generators. *Journal of Aircraft*, 24(5):305–309, may 1987.

[13] N. N. Sørensen, F. Zahle, C. Bak, and T. Vronsky. Prediction of the effect of vortex generators on airfoil performance. *Journal of Physics: Conference Series*, 524:012019, jun 2014.

[14] Y. He and Y. Zhang. Advances and outlooks of heat transfer enhancement by longitudinal vortex generators. In *Advances in Heat Transfer*, pages 119–185. Elsevier, 2012.

[15] P. Flohr and P. Stuttaford. Combustors in gas turbine systems. In *Modern Gas Turbine Systems*, pages 151–191e. Elsevier, 2013.

[16] G. M. Carlomagno and G. Cardone. Infrared thermography for convective heat transfer measurements. *Experiments in Fluids*, 49(6):1187–1218, aug 2010.

[17] L. A. Joseph, A. Borgoltz, and W. Devenport. Infrared thermography for detection of laminar-turbulent transition in low-speed wind tunnel testing. *Experiments in Fluids*, 57(5), apr 2016.

[18] Wheeler. Low drag vortex generators, 1991.

[19] T. Frey. *Numerische und experimentelle Untersuchungender 3D-Grenzschichtströmung in Wandnähe hochumlenkender Tandem-Gitter*. PhD thesis, Technical University of Kaiserslautern, 2014.

[20] R. B. Langtry and F. R. Menter. Correlation-based transition modeling for unstructured parallelized computational fluid dynamics codes. *AIAA Journal*, 47(12):2894–2906, dec 2009.

[21] T. T. Bisel, J. L. Dahlberg, T. R. Martin, S. S. Owen, R. G. Keanini, P. T. Tkacik, N. Narayan, and N. Goudarzi. A comparison of flat white aerosol and rhodamine (r6g) fluorescent paints and their effect on the results of tomographic PIV measurements. In *Volume 7: Fluids Engineering*. American Society of Mechanical Engineers, nov 2017.